Spectral and temporal measurements of the third-order nonlinear susceptibility of $LiNbO_3$ using picosecond Raman-induced phase-conjugation spectroscopy

P. J. Delfyett,* R. Dorsinville, and R. R. Alfano
Institute for Ultrafast Spectroscopy and Lasers, Department of Electrical Engineering, The City College of the City University, New York, 138th Street and Convent Avenue, New York, New York 10031
(Received 3 October 1988; revised manuscript received 13 March 1989)

Spectral and temporal measurements of the third-order nonlinear susceptibility were performed over 700 cm^{-1} in $LiNbO_3$ with use of Raman-induced phase-conjugation spectroscopy. Strong resonant enhancement was observed at six known vibrational frequencies, exhibiting relaxation times of less than 2 psec. These measurements show that $LiNbO_3$ has the potential to be used in ultrafast real-time optical processing systems, which require a large and fast $X^{(3)}$ optical nonlinearity.

INTRODUCTION

Fundamental nonlinear-optical studies are needed to find the ultimate material to implement in an optical computational system. Nonlinear optical four-wave-mixing techniques are becoming the preferred method for obtaining fundamental kinetic information about the third-order nonlinear susceptibility $X^{(3)}$ in condensed matter.[1] The Raman-induced phase-conjugation spectroscopy (RIPS) technique has been chosen in this study, as opposed to the older four-wave-mixing spectroscopic techniques, because the geometrical configuration of RIPS relaxes the phase-matching requirements so that broadband phase-matched Raman spectra can be obtained in isotropic or anisotropic materials with a single laser pulse, and the RIPS technique enables the measurement of the temporal response of the third-order susceptibility in real time with a single laser pulse with a temporal resolution of 2 psec.

Time-resolved Raman-induced phase-conjugation spectroscopy[2,3] is used to measure the components of the nonlinear third-order susceptibility $X^{(3)}$ as a function of frequency from 100 to 700 cm^{-1} in $LiNbO_3$. $LiNbO_3$ is shown to exhibit several resonantly enhanced peaks in the phase-conjugate spectrum having subpicosecond relaxation times. The temporal response of the resonant mode at 636 cm^{-1} was measured to be less than 2 psec using RIPS in conjunction with a streak-camera system.

EXPERIMENTAL METHOD

The experimental configuration utilized *nondegenerate* four wave mixing in the phase-conjugate geometry and is displayed in Fig. 1. Two laser pulses at frequency ω and $\omega-\Omega$, interacting at a large angle, $\sim 170°$, create a nonlinear polarization at the difference frequency Ω, where Ω is a molecular or optical-phonon vibration. A third laser beam at frequency ω enters the sample in a direction counterpropagating to $\omega-\Omega$. A portion of this beam is scattered into the phase-conjugate direction, which is frequency-shifted to the Stokes frequency $\omega-\Omega$. Normally this type of interaction is weak; however, due to the resonant enhancement of the third-order susceptibility at the vibrational frequency a large scattering efficiency is obtained.[4]

The laser pulses used in the experiment were produced from a Quantel neodymium-doped yttrium aluminum garnet (Nd:YAG) laser. The temporal duration of the laser pulses are ~ 30 psec at the second harmonic frequency. The maximum pulse energy used in the experiment is 10 mJ at 532 nm. 30% of the laser was split to create two 532-nm laser pulses. The remaining energy was used to pump a 5-cm continuum cell containing H_2O. The resulting white light generated from the continuum cell spanned the entire visible spectrum. The advantage of using this continuum light source is that it will couple to all Raman-active phonon modes which lie within the bandwidth of the continuum and also provides a shorter pumping pulse duration.[5] For vibrational frequencies ranging from 0 to 3000 wave numbers, the cor-

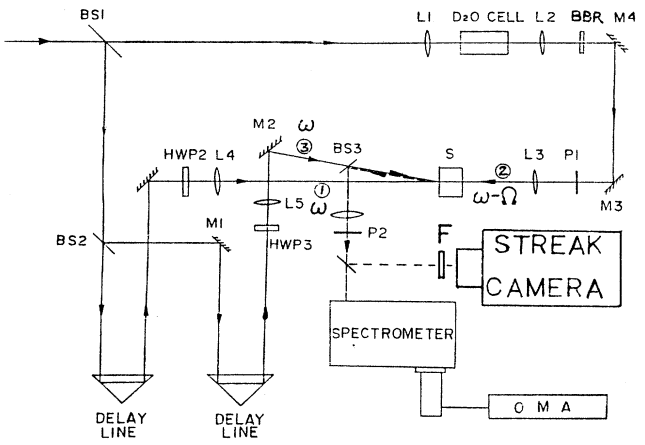

FIG. 1. Experimental setup used for measuring the Raman-induced phase-conjugate spectrum and the temporal response of individually selected modes. BS, beam splitter; M, mirror; HWP, half-wave rotator; P, polarizer; L, lens; S, sample; OMA, optical multichannel analyzer; BBR, broadband rotator; F, filter.

responding phonon **k** vectors range between 37 500 and 34 500 cm^{-1}.

The two 532-nm pulses entered the $LiNbO_3$ at an angle of 10°. The continuum was directed counterpropagating to one of the 532-nm laser pulses. Half-wave plates were inserted into the beam paths of the 532-nm pulses to control the polarizations. A broadband rotator and polarizer was inserted in the beam path of the continuum when different continuum polarizations were desired. A portion of the phase-conjugate signal was directed through an analyzer and into a 1-m spectrometer ($\sim$ 600-line/mm grating spacing) coupled with an OMA II detector system. By properly adjusting the input and output polarizations and the crystal orientation, the frequency dependence of the individual components of the nonlinear susceptibility can be measured.

Temporal measurements were obtained by directing a small amount of the phase-conjugate signal into a Hamamatsu 2-psec streak camera. The key feature which enables the vibrational dephasing time to be measured with a streak camera is the ultrashort temporal duration of the continuum, $\sim$2 psec.[5] The temporal profile of the detected pulse contains contributions from the electronic and vibrational components of the third-order susceptibility. When the vibrational lifetime is longer than the duration of the continuum pulse but shorter than the probing pulse duration, the scattered pulse envelope will decay exponentially in real time at exp $(-2t/\tau)$, where τ is the dephasing time of the coherent vibrations.

EXPERIMENTAL RESULTS

The RIPS signal was measured for various combinations of input polarization and crystal orientations. Several single-shot spectra were recorded and averaged to eliminate spectral fluxuations in the continuum generation process.

A typical RIPS spectra is shown in Fig. 2(a) for the condition where all three input laser pulse polarizations are vertical and parallel to the crystal optic axis, or z axis. The RIPS scattered spectra are also z polarized. The nonlinear third-order susceptibility responsible for the spectra is $(X^{(3)})_{zzzz}$, which shows three resonantly enhanced peaks in the output spectrum. These peaks correspond to the three strongest Raman-active $A_1(z)$ modes. The spectral asymmetry observed in the line shapes is attributed to an interaction between the resonant and the nonresonant electronic and nuclear background components of $X^{(3)}$.

In Fig. 2(b) the input polarization of the two-532-nm laser pulses are oriented perpendicular to the z axis. The continuum pulse and phase-conjugate signal are vertically polarized along z. The third-order susceptibility for this configuration corresponds to $(X^{(3)})_{zyzy}$. Three Raman peaks are observable which will be shown to correspond to the strongest E-type Raman-active modes. The asymmetry of the line shapes in this spectra is more pronounced. It will be shown that this is due to a decrease of the relative strengths of the Raman-active modes with respect to the nonresonant electronic and nuclear background of $X^{(3)}$.

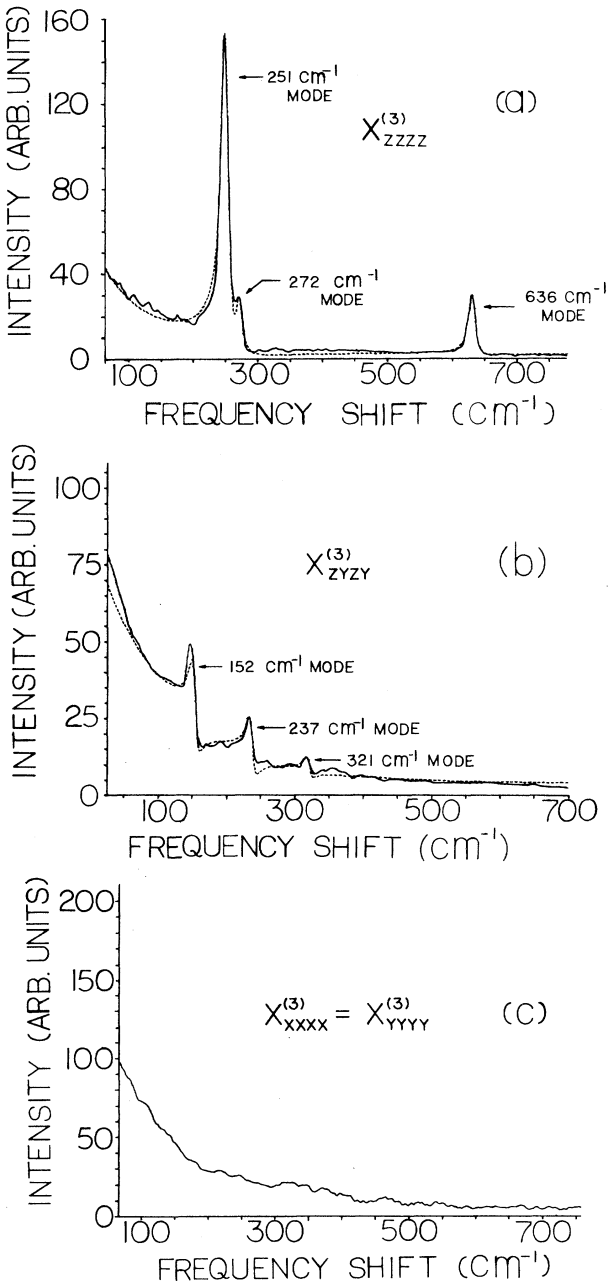

FIG. 2. (a) RIPS third-order susceptibility spectra for the *zzzz* component. The linewidths, vibrational frequencies, and oscillator strengths used in the calculation are listed in Table I. The parameters used to model the continuum background are given in the text. (b) RIPS third-order susceptibility spectra for the *zyzy* component. The linewidths, vibrational frequencies, and oscillator strengths used in the computer calculation are tabulated in Table I. The parameters used to model the continuum background are given in the text. (c) RIPS third-order susceptibility spectra for the *xxxx* = *yyyy* component. No observable resonant enhancement due to Raman vibrations is obtained with this polarization configuration. The resulting scattered spectrum is just composed of nonresonant nuclear and electronic interactions. The intensity of the spectrum vs frequency gives a measure of the intensity variation of the continuum pulse used in the experiment.

In Fig. 2(c) all three input pulses are vertically polarized; however, the crystal was rotated so that the polarization vectors are parallel to the x or y axis. The output spectrum is also vertically polarized. This configuration corresponds to a scattered spectrum which is due to $(X^{(3)})_{xxxx}=(X^{(3)})_{yyyy}$. In this spectra, no noticeable Raman lines are observed. The scattered spectrum is primarily due to the nonresonant electronic and nuclear terms. The measured intensity variation of the scattered signal versus wavelength is due to the intensity variation of the continuum versus wavelength.

Other combinations of input polarization were also employed; however, no additional Raman lines were observed. The salient features of these spectra showed either a flat background or a continuum background similar to the spectra shown in Fig. 2(b).

In Fig. 3 the temporal evolution of the resonant mode at 636 cm^{-1} is displayed. The temporal evolution is obtained by directing the RIPS spectra through a 10-nm bandpass filter centered at 550 nm, and then detected with a 2-psec Hamamatsu streak camera. The temporal evolution of the RIPS scattered pulse shows a response which is unresolved and limited to the response of the streak camera, ≤ 2 psec.

THEORY

In this section the theory to describe the above data is given. The third-order nonlinear polarization is given by

$$P_i^{(3)}=X_{ijkl}^{(3)}E_jE_kE_l^* \ , \tag{1}$$

where $X_{ijkl}^{(3)}$ is the third-order susceptibility. For anisotopic materials there are 81 elements implied by Eq. (1) which can be reduced by considering the specific crystal class. Lithium niobate belongs to the C_{3v} trigonal crystal class. The number of nonzero elements in $(X^{(3)})_{ijkl}$ reduces to 37, with 14 independent components. Following the notation of Hellwarth,[16] the reduced form of the susceptibility, h_{ijkl}, can be employed. The symmetry properties of the reduced susceptibility obey the relation

$$h_{ijkl}=h_{jikl}=h_{ijlk}=h_{jilk}=h_{klij} \ .$$

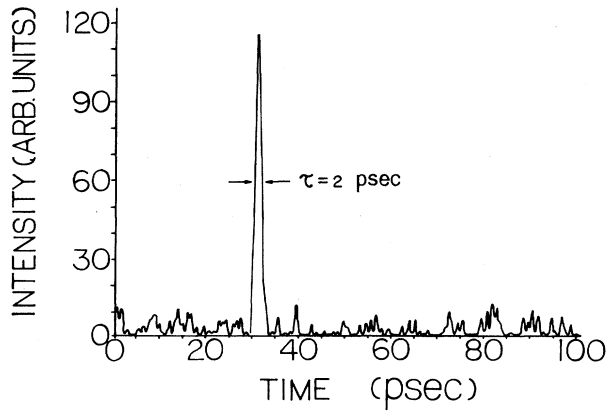

FIG. 3. Temporal response of the 630-cm^{-1} mode, showing a dephasing time limited by the resolution of the streak camera, ≤ 2 psec.

Using these relations, the 14 independent components of $X_{ijkl}^{(3)}$ can be reduce to six independent components of h_{ijkl}. Each of these six independent components of h_{ijkl} has an associated impulse response, $h_{ijkl}(t)$, which is essentially the impulse response of the nucleus to an applied external electric field. These nuclear impulse response functions for the six $h_{ijkl}(t)$ are denoted as $a(t),b(t),\ldots,f(t)$.

The third-order susceptibility X_{ijkl} can now be given as a function of frequency in terms of the electronic, and nonresonant and resonant nuclear components, such that

$$X_{ijkl}^{(3)}(\omega_L-\omega_S)\rightarrow\sigma_{ijkl}+H_{ijkl}(0)+H_{ikjl}(\omega_l-\omega_S) \ . \tag{2}$$

Here, σ is the electronic contribution, and $H(0)$ and $H(\omega_L-\omega_S)$ are related to the Fourier transforms of the reduced susceptibility response functions, $h_{ijkl}(t)$,

$$H_{ijkl}(\Delta)=\frac{1}{2\pi}\int_0^\infty h_{ijkl}(t)\exp(-i\Delta t)dt$$

$$\text{where } \Delta=\omega_L-\omega_S \ . \tag{3}$$

Here, $H(0)$ is the frequency-independent nuclear component, while $H(\omega_L-\omega_S)$ is the resonant nuclear component.

Using the above relation for $X^{(3)}$ in Eq. (2), the 14 independent third-order susceptibility components versus frequency can be given as

$$X_{zzzz}=\sigma+A(0)+A(\Delta) \ , \tag{4a}$$

$$X_{xxyy}=\sigma+B(0)+C(\Delta) \ , \tag{4b}$$

$$X_{xyxy}=\sigma+C(0)+B(\Delta) \ , \tag{4c}$$

$$X_{xyyx}=\sigma+C(0)+C(\Delta) \ , \tag{4d}$$

$$X_{yyzz}=Z_{zzyy}=\sigma+D(0)+E(\Delta) \ , \tag{4e}$$

$$X_{zyyz}=X_{yzzy}=\sigma+E(0)+E(\Delta) \ , \tag{4f}$$

$$X_{yzyz}=X_{zyzy}=\sigma+E(0)+D(\Delta) \ , \tag{4g}$$

$$X_{yyyz}=X_{yyzy}=X_{yzyy}=X_{zyyy}=\sigma+F(0)+F(\Delta) \ . \tag{4h}$$

In these equations σ is the electronic contribution and the quantities $A,B,\ldots,F$ are the Fourier transforms of the nuclear response functions for the six independent components of the reduced susceptibility h_{ijkl}, with 0 and Δ the frequency-independent and -dependent components, respectively. By measuring the RIPS spectra versus frequency with properly aligned input and output polarizations, specific components of the third-order susceptibility can be measured. Vibrational frequencies, linewidths, and relative strengths of the resonant and nonresonant components can also be determined.

DISCUSSIONS

The expressions in the above equations can be related to the standard Raman tensor $R_{\sigma\rho}$, to verify the selection rules and determine the symmetry type of the optical-phonon modes which are being coherently driven in the RIPS technique. For $LiNbO_3$, the Raman tensor $R_{\sigma\rho}$ are[7]

$$\begin{bmatrix} a & 0 & 0 \\ 0 & a & 0 \\ 0 & 0 & b \end{bmatrix} \text{ for } A_1(z), \quad \begin{bmatrix} 0 & -c & -d \\ -c & 0 & 0 \\ -d & 0 & 0 \end{bmatrix} \text{ for } E(-x), \quad \begin{bmatrix} c & 0 & 0 \\ 0 & -c & d \\ 0 & d & 0 \end{bmatrix} \text{ for } E(y) . \tag{5}$$

The A and E matrices denote the symmetry type of the excited phonon mode. The x, y, and z correspond to the polarization of the phonon, and the coefficients a, b, c, and d are the coupling coefficients between the incident electric field with polarization σ and the scattered Stokes wave with polarization ρ. The scattering efficiency can be written as

$$S = \sum_{\sigma,\rho} (A e^i_\sigma R_{\sigma\rho} e^s_\rho)^2 . \tag{6}$$

In Fig. 2(a) the input polarizations for all three input pulses are polarized parallel to the crystal optic axis, i.e., z polarized. The output polarization is also z polarized. By examining the above scattering matrices, the only term which can contribute an incident z-polarized wave to scatter into a z-polarized Stokes wave is an $A_1(z)$ mode with coupling coefficient b.

Physically, this case corresponds to the creation of a coherent phonon population by the production of an intensity grating due to the interference of ω_L and ω_S. The phonon $\mathbf{k}$ vector is identical to the grating $\mathbf{k}$ vector, i.e.,

$$\mathbf{k}_{\text{grating}} = \mathbf{k}_{\text{phonon}} = \mathbf{k}_{\text{laser}} - \mathbf{k}_{\text{Stokes}} .$$

This intensity grating is not static as in the conventional degenerate phase-conjugation scheme, but it drifts with a velocity $\mathbf{v}$ which is a function of the frequency difference $\omega_L - \omega_S = \Omega$, and the crossing angle of the two beams. The grating $\mathbf{k}_g$ vector and the velocity adjust itself so that the product equals the phonon frequency, i.e., $\Omega = \mathbf{v}\cdot\mathbf{k}_g$. For a crossing angle of 170° in the sample, and pumping wavelengths of $\lambda_L = 530$ nm and $\lambda_s = 550$ nm ($\Omega = 686$ cm^{-1}), typical grating wavelengths $\Lambda = 2\pi/|\mathbf{k}|$ and velocities are 271 nm and 5.5×10^8 cm/sec, respectively. The phonon polarization for this situation is also z polarized due to the polarization of the interfering laser pulses and the moving intensity grating.

In the four-wave-mixing terminology, this scattering takes place through

$$(X^{(3)}_{zzzz}) = \sigma + A(0) + A(\Delta) ,$$

where σ and $A(0)$ are the nonresonant components of the susceptibility $X^{(3)}$, $A(\Delta)$ is the resonant component, $X^{(3)}_{\text{RES}}$. In Fig. 2(a) the resonances due to $A(\Delta)$ are clearly observable. In addition, an interference between σ, $A(0)$, and $A(\Delta)$ is observed, which gives rise to the asymmetric line shapes in the scattered spectra. The variation of the nonresonant background is due to the variation of the continuum pulse E_2 versus wavelength. The fitting to the spectra will be described in the next section to determine the values of σ, $A(0)$, and $A(\Delta)$.

The spectra in Fig. 2(b) utilize input polarizations of $E_1 = y$, $E_2 = z$, and $E_3 = y$, with an output polarization $E_4 = z$. The only possible modes which can scatter a y-polarized laser wave to a z-polarized Stokes wave are the E-type phonon modes, with a coupling coefficient $R_{yz} = d$. The E modes have polarizations which lie in the x,y plane. This can be understood by examining the instantaneous electric field which is produced by the interference of the pumping Stokes and laser waves. Since these two pulses are orthogonally polarized, no real intensity modulation is created. The intensity distribution is uniform, however, and the instantaneous electric field polarization created by E_L and E_S rotates in a plane perpendicular to $\mathbf{k}_L - \mathbf{k}_S$. This rotating motion occurs at a frequency $\omega_L + \omega_S$. However, there is a low-frequency modulation impressed on this motion at $\omega_L - \omega_S = \Omega$. This low-frequency modulation is responsible for the displacement of the atoms in the plane perpendicular to the z axis. This motion creates phonons polarized in the x,y plane. The spectra in Fig. 2(b) are due to E-type phonon modes. This orthogonal polarization scheme becomes a way to selectively drive E-type phonon modes. The motion of the displaced atoms induces a change in the nonlinear refractive index. Once a periodic modulation of the refractive index is established, the concept of the dynamical moving grating can then be used as a physical description for the light-scattering process.

Relating the spectra of Fig. 2(b) to the nonlinear third-order susceptibility shows that terms similar to $yzyz = zyzy$ are responsible for the scattered spectrum. This component is related to $\sigma + E(0) + D(\Delta)$. The resonant terms are clearly observable, and are superimposed on a nonresonant background. The intereference between the resonant and nonresonant components are also observable and the interference effect is more pronounced.

In Fig. 2(c) the crystal was rotated by 90°, with the input polarizations oriented in the same fashion as in the spectra of Fig. 2(a), i.e., vertically polarized. The scattered spectra are also vertically polarized. This polarization configuration couples the scattered wave to the input laser pulses through $xxxx = yyyy$. With these input and output polarizations, no noticeable resonantly enhanced vibrational lines are observed. In the four-wave-mixing notation, this spectrum is produced through the coupling coefficient of $(X^{(3)})_{xxxx} = (X^{(3)})_{yyyy}$. Since

$$X_{xxxx} = X_{yyyy} = X_{xxyy} + X_{xyyx} + X_{xyxy} ,$$

we see that the spectra in Fig. 2(c) correspond to $3\sigma + B(0) + B(\Delta) + 2C(0) + 2C(\Delta)$. Since there is no resonantly enhanced vibrational lines in the observed spectrum, we can conclude that the frequency-dependent components, $B(\Delta)$ and $C(\Delta)$, which give rise to the resonantly enhanced vibrational lines, are small. The scattered spectrum is just due to $3\sigma + B(0) + 2C(0)$, the nonresonant background terms. These spectra, since they only involve nonresonant terms, give a measure of the spectral distribution of the continuum. These spectra can then be used as a measure of the nonresonant background

spectra, which are present in spectra of both Figs. 2(a) and 2(b). In this case, since $(X^{(3)})_{xxxx}=(X^{(3)})_{yyyy}$, the resulting scattered spectra are identical for a 90° rotation in a plane perpendicular to the z axis. However, when comparing the $xxxx$ and $yyyy$ spectra to the standard Raman tensor, some difficulty arises in determining the standard Raman coupling coefficient. This is easily seen by the fact that the $xxxx$ spectrum gives information about phonons which are $\hat{\mathbf{x}}$ polarized, i.e., $E(-x)$ modes, where the incident and scattered light is also x polarized. This type of interaction is not allowed by the selections rules. However, the $yyyy$ spectrum gives information about phonons which are y polarized, i.e., $E(y)$ modes, where the incident and scattered light is y polarized. This type of interaction is allowed by the selection rules, where the coupling coefficient $R_{\sigma\rho}$ is c. In order to obtain a better understanding and interpret the experimentally measured spectrum, the previously measured spontaneous Raman spectrum can be consulted.[8] The spectra in Ref. 8 show two weak modes at 610 and 878 cm^{-1} for a polarization configuration which allows Raman scattering through $E(y)$-type phonon models with coupling coefficient $R_{\sigma\rho}=c$. Both of these modes have been identified as mixed phonon modes.[8] These modes are most likely not observed in our spectrum due to the small signal intensity produced by these modes and the weak continuum pulse which is used to drive these modes. In addition, the mixed modes are probably less effective than the pure TO modes which are excited in this experiment. These arguments offer possible explanation of why the vibrational lines at 610 and 878 cm^{-1} are not observed in our spectrum as compared to the results of Ref. 8. However, a definitive explanation requires more depth in theory.

SPECTRAL ANALYSIS

In order to extract physical parameters from the observed experimental spectra, a model is proposed for the nonlinear third-order susceptibility. Since the experiment measures the resonant enhancement due to nuclear motions, a sum of Raman Lorentzian line shapes is assumed:

$$X^{(3)}_{\mathrm{RIPS}}(\omega_L-\omega_S)=X^{(3)}_{\mathrm{nr}}+\sum_{i=1}^{N}\frac{a_i}{(\omega_l-\omega_S-\Omega_i)+i\Gamma_i}\ , \tag{7}$$

where

$$(X^{(3)}_{\mathrm{nr}})_{ijkl}=\sigma_{ijkl}(0)+H_{ijkl}(0) \tag{8}$$

and

$$H_{ikjl}(\omega_L-\omega_S)=\sum_{i=1}^{N}\frac{a_i}{(\omega_L-\omega_S-\Omega_i)+i\Gamma_i}\ . \tag{9}$$

In these equations, a_i, Ω_i, and Γ_i are the oscillator strength, vibrational frequency, and linewidth [half-width at half maximum (HWHM)] of the ith mode, and $X^{(3)}_{\mathrm{nr}}$ is the nonresonant background contribution, which is composed of both nonresonant electronic and nuclear contributions. The scattered signal is proportional to $|X^{(3)}|^2$.

It is interesting to note the different contributions which give rise to the scattered spectra. The first type of contribution occurs from the purely nonresonant background terms, i.e., $X^{(3)}_{nr}$. The second type of process contributes an *interference term* which is due to the interaction between the nonresonant electronic background and individual vibrational resonant terms, i.e., $X^{(3)}_{\mathrm{nr}}$ and a_i. The third type of contribution comes from individual resonances, a_i, and the fourth type of term from an *interference between two different resonant modes*, a_i and a_j.

Using the spectra of Fig. 2(c) as a measure of the frequency variation of the nonresonant background and continuum variation for $X^{(3)}_{\mathrm{nr}}$ in Eq. (6), the spectra of Figs. 2(a) and 2(b) can be modeled by varying the relative oscillator strengths, vibrational frequencies, and linewidths.

The resulting theoretical spectra using the above model are shown as the dotted curves in Figs. 2(a) and 2(b). The nonresonant background due to the continuum variation versus wavelength was modeled as exponential "wings," after the spectra in Fig. 2(c). An additional constant background component was also added to the nonresonant background.

In Fig. 2(a) the vibrational frequencies which were used in the calculation were $\Omega=251$, 272, and 636 cm^{-1}. These frequencies are in excellent agreement with previously measured values.[8,9] The relative strengths of these three vibrational frequencies are $|a_1|=64$, $|a_2|=30$, and $|a_3|=32$. The value of the exponentially varying spectra was ~ 4.75 at $\Omega=100$ cm^{-1} and the dc term was 1.0. The value of the continuum linewidth is 165 cm^{-1}. The continuum linewidth gives a measure of the intensity variation of the continuum versus frequency. The vibrational linewidths used are $\Gamma_1=6$ cm^{-1}, $\Gamma_2=7.5$ cm^{-1}, and $\Gamma_3=6$ cm^{-1}. The extracted values for the linewidth and vibrational frequencies are in good agreement with previously measured values.[8,9] The extracted values from the computer fit are tabulated along with the previously measured values in Table I, for comparison.

From these linewidths, the dephasing times for these vibrations can be obtained, assuming a homogeneously broadened Lorentzian linewidth, i.e.,

$$\pi c\tau=(\delta\nu)^{-1}\ ,$$

where $\delta\nu$ is the linewidth [full width at half maximum (FWHM, i.e. 2Γ)] in units of wave numbers, c is the speed of light, and τ is the dephasing time. For the 636-cm^{-1} mode, a $\delta\nu$ of 6 cm^{-1} gives a dephasing time of ~ 440 fsec. This value is consistent with the unresolved dephasing measurement displayed in Fig. 3, which shows a temporal response faster than 2 psec.

The spectra in Fig. 2(b) were also modeled in the same fashion. The vibrational frequencies used in this model are $\Omega_1=152$ cm^{-1}, $\Omega_2=237$ cm^{-1}, and $\Omega_3=321$ cm^{-1}. These values of Ω are in excellent agreement with previously measured values.[8,9] The relative strengths of these modes are $|a_1|=14$, $|a_2|=12$, and $|a_3|=5$. The nonresonant background was modeled with a constant term of 1.97, a continuum linewidth of 170 cm^{-1}, and a strength of 6.15 at $\Omega=25$. The linewidths used in this calculation were $\Gamma_1=5$ cm^{-1}, $\Gamma_2=5$ cm^{-1}, and $\Gamma_3=4$ cm^{-1}. These linewidths imply dephasing times of 500

TABLE I. Table of the linewidths, vibrational frequencies, and oscillator strengths used to fit the experimentally observed Raman-induced phase-conjugate spectrum. Previously measured values are also listed and are in good agreement with the extracted parameters from the computer analysis. σ is the Raman-scattering cross section and $|\bar{a}_i|$ and $\bar{\sigma}$ have been normalized to the E mode at 321 cm^{-1}. Ω denotes vibrational frequency, Γ denotes the linewidth, a_i denotes vibrational oscillator strength, $\bar{a}_i$ denotes normalized vibrational oscillator strength, $X_{nr}^{(3)}$ denotes nonresonant third-order susceptibility, σ denotes the Raman cross section, and $\bar{\sigma}$ denotes the normalized Raman cross section.

Vibrational frequencies, linewidths, and relative strengths								
This work					After Refs. 8 and 9			
Ω (cm^{-1})	Γ (cm^{-1})	$\lvert a_i \rvert$	$\lvert \bar{a}_i \rvert$	$\lvert a/X_{nr}^{(3)} \rvert$	Ω (cm^{-1})	Γ (cm^{-1})	σ	$\bar{\sigma}$
152 (E)	5	14	2.8	2.8	151	4	3.8	3.95
237 (E)	5	12	2.4	3.2	237	4	2.9	3.02
251 (A_1)	6	64	12.8	22	253	7.5	16	16.66
272 (A_1)	7.5	30	6	11	278	4	4.0	4.1
321 (E)	4	5	1	1.6	321	3	.96	1
636 (A_1)	6	32	6.4	27	637	7.5	10	10.4

fsec for the 152- and 237-cm^{-1} modes, and 650 fsec for the 321-cm^{-1} mode. These times are also faster than our 2-psec time-resolution technique.

The values of a_i used in the calculation represent the oscillator strengths and are related to the spontaneous Raman-scattering cross section. If the extracted values of a_i from the computer fit are normalized to a standard reference value, then a comparison can be made to the previously measured values of the spontaneous Raman-scattering cross section. The extracted a_i's and the previously measured spontaneous Raman-scattering cross section σ were normalized to the weakest E mode at 321 cm^{-1}. Comparing the extracted and normalized $\bar{a}_i$'s from the computer fit with the normalized values of the spontaneous Raman scattering cross section $\bar{\sigma}$ from Ref. 9 shows good agreement between the two measurements. These results are listed in Table I, for comparison.

To obtain values of the nonresonant third-order susceptibility, the ratio $|a_i/X_{nr}^{(3)}|$ is calculated from the computer fit. Absolute measurements of the intensities used in the experiment are difficult to obtain. However, the relative values of the resonant and nonresonant components are easily extracted from the computer fit. Typical relative values between $|a_i|$ and $X_{nr}^{(3)}$ varied between 1.6 and 27. Once the ratio of $|a_i/X_{nr}^{(3)}|$ is known, the nonresonant third-order susceptibility is calculated by using the values of the spontaneous Raman cross section σ for a_i.

The slight differences between the linewidths measured with this technique compared with other works can be attributed to the linewidths' dependence on phonon **k** vector, which is due to phonon dispersion. In the previous investigations,[8,9] the typical phonon wave vector is roughly equal to the incident and scattered photon wave vector, for 90° Raman scattering. In our investigation, the typical phonon wave vector is close to twice the photon wave vector, because the pumping pulses interact in an almost counterrunning geometry. This large difference in phonon **k** vector puts the interaction at different points on the dispersion curve, thus giving slightly different values of the linewidths and vibrational frequencies.

SUMMARY

Our work shows that $LiNbO_3$ exhibits several vibrational frequencies which couple efficiently to the third-order nonlinear susceptibility. These modes can be selectively driven with proper input pulse polarizations. The resulting linewidths are relatively narrow and exhibit subpicosecond dephasing times. The nonlinear third-order susceptibility of $LiNbO_3$ as a function of frequency from $\sim$75 to $\sim$700 cm^{-1} using RIPS was measured. Six strong resonantly enhanced peaks were observed in the phase-conjugate output spectrum. Typical enhancement factors ranged from 5 to 30 times. The peak positions were consistent with previously measured spontaneous Raman vibrational spectra. RIPS selection rules were verified and specific components of the third-order susceptibility were identified with the corresponding Raman spectrum. The output spectrum was modeled using a sum of Raman oscillators along with a nonresonant background term. Relative strengths of the individual components were obtained, along with the vibrational frequencies and the linewidths by fitting the experimental spectra. Values of the nonresonant component of the third-order susceptibility are extracted from the analysis. The extracted linewidths imply subpicosecond dephasing times, which were consistent with the real-time phonon dephasing measurement for the 636-cm^{-1} mode.

ACKNOWLEDGMENTS

We thank Capt. M. Malloy and Dr. L. Giles for their encouragement and support of the U.S. Air Force Office of Scientific Research under (AFOSR) Grant No. 86-0144. This work is in partial fulfillment of the Ph.D. requirement for one of us (P.D.).

*Present address: Bell Communications Research, Inc. (Bellcore), P.O. Box 7020, Red Bank, NJ 07701-5699.

[1]*Principles of Nonlinear Optics,* edited by Y. R. Shen (Wiley Interscience, New York, 1985).
[2]S. K. Saha, and R. W. Hellwarth, Phys. Rev. A **27**, 919 (1983).
[3]R. Dorsinville, P. J. Delfyett, and R. R. Alfano, Appl. Opt. **26**, 3655 (1987).
[4]P. J. Delfyett, R. Dorsinville, and R. R. Alfano, Opt. Lett. **12**, 1002 (1987).
[5]R. Dorsinville, P. J. Delfyett, and R. R. Alfano, Appl. Opt. **27**, 16 (1988).
[6]R. W. Hellwarth, Prog. Quantum Electron. **5**, 1 (1977).
[7]R. Loudon, Adv. Phys. **13**, 423 (1964).
[8]A. S. Barler and R. Loudon, Phys. Rev. **158**, 433 (1967).
[9]I. P. Kaminow and W. D. Johnston, Jr., Phys. Rev. **160**, 519 (1967).